Chapter 5
Experimental Optimization of Propagation-Based BCT

Effective design and implementation of a propagation-based CT setup require careful optimization both in terms of physical parameters (hardware) and data processing (software). The goal of the present chapter is to describe and provide a scientific justification for several of these aspects, combining a theoretical/mathematical background with experimental results in the context of the SYRMA-3D project. Specifically, in the first two sections a model describing the propagation of signal and noise through the imaging chain will be introduced; by comparing experimental data with theoretical predictions, the effects of propagation distance and detector pixel size on image noise and signal-to-noise-ratio will be discussed and the consequences of these findings on the SYRMEP beamline upgrade will be presented. In the third section the development of a beam filtration system to produce a vertically wider and more uniform X-ray intensity distribution at the sample position will be described. In the fourth and last section a post-reconstruction phase-retrieval pipeline, aiming at compensating for periodic artifacts arising in multi-stage CT acquisitions, will be introduced, also providing a mathematical proof of the equivalence to its pre-reconstruction counterpart.

5.1 The Effect of Propagation Distance

As PB imaging relies on the free-space propagation of the perturbed X-ray wavefront between the object and the detector, it is not surprising that the object-to-detector (or propagation) distance plays a crucial role in determining the final image appearance, as already mentioned in Sect. 2.2. For this reason, a formal model describing the effect of propagation distance on image quality metrics as noise, signal-to-noise ratio (SNR) and spatial resolution is introduced in this section and applied to the specific case of

L. Brombal, *X-Ray Phase-Contrast Tomography*, Springer Theses,
https://doi.org/10.1007/978-3-030-60433-2_5

PBBCT. The model is mainly derived from theoretical works by Iakov I. Nesterets and Timur Gureyev [1, 2]. Comparisons between theory and experimental results will be shown in the next sections, and the impact of the findings on the upgrade of the experimental setup will be discussed.

5.1.1 Theoretical Model

In Sect. 2.4 the propagation process has been described as an operator acting on the X-ray intensity distribution emerging from the object at the object plane. To take into account the realistic case of a divergent beam, where the geometrical magnification M is not negligible, the (forward) propagation operator previously introduced has to be slightly modified to

$$H' = \left(1 - \frac{z_1}{M}\frac{\delta}{2k\beta}\nabla_{xy}^2\right) = \left(1 - \frac{z'\lambda\delta}{4\pi\beta}\nabla_{xy}^2\right) \tag{5.1}$$

where $z' = z_1/M$ is referred to as effective propagation distance and the definition $k = 2\pi/\lambda$ has been inserted. This equation implies that phase-contrast signal appears at the interfaces of/within the imaged object, where the intensity Laplacian is expected to be significantly different from zero, and it is proportional to the propagation distance. On the contrary, within uniform regions of the collected image (i.e. far from sharp details) the Laplacian term can be neglected and the detected signal only depends on the attenuation properties of the object. For this reason, if measured far from sharp interfaces where phase-contrast is present, neither the (large-area) signal nor the statistical noise (that, in case of Poissonian statistics, is proportional to the square root of the signal) are affected by the propagation process. The same consideration holds also for the image (large-area) contrast, that is defined as the difference between a detail and background signals, measured far from interfaces, normalized to the background.

5.1.1.1 Effects on Spatial Resolution

As stated previously, while not affecting large-area signal and noise, propagation produces the edge-enhancement effect which boosts the high spatial frequency component of the image, hence improving the spatial resolution. To understand this effect quantitatively, let us define the image blur in a planar image, which is inversely proportional to the spatial resolution, as the standard deviation of the detector PSF (here the source is assumed to be point-like) considering, for the sake of simplicity, the mono-dimensional case

$$(\Delta x)\,[\mathrm{PSF_{det}}] = \left(\int x^2 \mathrm{PSF_{det}}(x)\,\mathrm{d}x \right)^{1/2} \tag{5.2}$$

Starting from this definition it can be demonstrated that, by applying the propagation operator introduced in Eq. (5.1), the effective detector PSF width is decreased in the propagation process, i.e. the spatial resolution is improved [2]:

$$(\Delta x)^2_{z'}\,[\mathrm{PSF_{det}}] = (\Delta x)^2\,[\mathrm{PSF_{det}}] - \frac{z'\lambda\delta}{2\pi\beta} \tag{5.3}$$

Of note, the last term of the equation, determining the narrowing of the effective PSF, depends linearly on the effective propagation distance.

The propagation process is followed by the application of the phase-retrieval algorithm. As described in Sect. 2.4, the PhR is a low-pass filter, thus it affects the image by reducing noise and degrading the spatial resolution. Following the same line of reasoning used to describe the change in resolution due to the propagation, and recalling that the PhR operator is the inverse of the propagation operator, the application of PhR leads to an increase of the image blur that reads:

$$(\Delta x)^2_{\mathrm{PhR}}\,[\mathrm{PSF_{det}}] = (\Delta x)^2\,[\mathrm{PSF_{det}}] + \frac{z'\lambda\delta}{2\pi\beta} \tag{5.4}$$

where the term responsible for the PSF widening is the same as in Eq. (5.3) but with opposite sign. At this point it is clear that combining propagation and phase retrieval means to add and subtract the term $z'\lambda\delta/(2\pi\beta)$, thus leaving the spatial resolution unaltered. Since the latter statement is valid for each planar projection image, it is trivial to conclude that it applies also to the reconstructed tomographic volume.

5.1.1.2 Effects on Image Noise

Having shown that the effects of phase retrieval and forward propagation on spatial resolution exactly compensate each other, let us steer the attention on the effect of phase retrieval on CT image noise. A rather general model of image noise in reconstructed CT slices has been recently introduced by [3] and its formulation is well suited to include analytically the phase-retrieval filter.

According to the model, by assuming a Poisson dominated detector noise, flat-fielded bi-dimensional projection images, stable source intensity and imaging setup, and parallel beam tomographic reconstruction performed through the Filtered-Back-Projection (FBP) algorithm, the variance (var) in homogeneous region of a CT image is given by

$$\mathrm{var} = \frac{f(A; d/h) F_{\mathrm{obj}}}{N_p h'^4 \Phi \mathrm{DQE}_0 T_{\mathrm{obj\text{-}det}}} \tag{5.5}$$

where F_{obj} accounts for X-rays attenuation in the object, N_p is the number of projections in the tomographic scan, Φ is the X-ray fluence at the object (in number of photons per square millimeter), DQE_0 is the detector quantum efficiency at zero spatial frequency, $T_{\text{obj-det}}$ is the transmittance through the object-to-detector distance (usually transmission in air) and $h' = h/M$ is the effective pixel size accounting for the geometrical magnification M and it is assumed to be bi-dimensional with equal width and height. The dimensionless function $f(A; d/h)$ accounts for the tomographic process, the detector response and phase retrieval, and it is written as:

$$f(A; d/h) = 2\pi^2 \int_0^{\frac{1}{2}} \mathrm{d}U G^2(U) F_{\text{interp}}(U) \int_{-\frac{1}{2}}^{\frac{1}{2}} \mathrm{d}V \frac{\text{MTF}^2(U, V; d/h)}{\left[1 + 4A\left(U^2 + V^2\right)\right]^2} \quad (5.6)$$

Here $G(U)$ is the the CT filter, $F_{\text{interp}}(U)$ describes the effect on noise of the interpolation from polar to Cartesian coordinates in the backprojection process, $\text{MTF}(U, V; d/h)$ is the detector planar modulation transfer function parametrized through the dimensionless quantity d/h, where d is the full width at half maximum (FWHM) of the detector's point spread function. Of note, the integration variables U and V are dimensionless normalized frequencies expressing the fraction of twice the maximum detected frequency (Nyquist frequency), hence fractions of $(h/M)^{-1}$. Finally, the dimensionless parameter A depends on the refractive properties of the sample, on the setup geometry and on the detector pixel size as

$$A = (\pi/4)\frac{z'\lambda\delta}{h'^2\beta} \quad (5.7)$$

where δ/β can be referred to both single- and two-materials phase retrieval (see Sect. 2.5).

Despite its rather complex formulation, the function f is key in understanding the effect of phase retrieval on image noise which is summarized in the denominator of Eq. (5.6). In facts, when no PhR is applied $A = 0$ and, as a consequence, the function f does not explicitly depend neither on the effective propagation distance nor on the effective pixel size: in this case, following Eq. (5.5), the image noise ($\sigma = \sqrt{\text{var}}$) at fixed sample fluence is found to be proportional to $1/h'^2 = M^2/h^2$, which is a known result in the context of conventional CT [4]. On the contrary, if PhR is applied $A > 0$ and the denominator in Eq. (5.6) is larger than 1, hence the function f gets smaller if compared with the case $A = 0$, bringing to a reduction in image noise. More in detail, an increase of propagation distance and/or a decrease on the effective pixel size, bring to an increase of the parameter A which, in turn, determines a decrease in image noise.

If we define σ_{PhR} and σ_{noPhR} to be the noise in a flat region of a tomographic image obtained with and without the application of PhR, respectively, the noise reduction factor associated to PhR can be written as

$$\frac{\sigma_{\mathrm{PhR}}}{\sigma_{\mathrm{noPhR}}} = \left[\frac{f(A; d/h)}{f(0; d/h)}\right]^{1/2} \tag{5.8}$$

In general, this factor cannot be calculated analytically as to compute the function f considering a realistic MTF, reconstruction filters and interpolations numerical integration is required: these realistic parameters will be introduced in the next section. Anyway, following the work by Nesterets and colleagues [1], an explicit analytical formula can be found by assuming a flat detector MTF up to the Nyquist frequency, a ramp tomographic filter, the use of nearest neighbour interpolation and large values of A ($A \gg 1$):

$$\frac{\sigma_{\mathrm{PhR}}}{\sigma_{\mathrm{noPhR}}} = \left[\frac{3\pi}{8}\frac{\ln A - 1}{A^2}\right]^{1/2} \tag{5.9}$$

Of course, considering the simplifications introduced in describing both the detector and the tomographic reconstruction process, this equation has to be regarded as a first approximation providing a rough estimate of the noise-reduction factor. On the other hand, in the specific case of the SYRMA-3D BCT project, the assumption $A \gg 1$ is rather reasonable since $z' > 1$ m, $h' \sim 50$ μm, $\delta/\beta \sim 10^3$ and $\lambda \sim 3 \cdot 10^{-11}$m, yielding $A \gtrsim 10$.

At this point, recalling that large-area signal is not altered by the application of the PhR, as shown in Fig. 5.1, and by defining the signal-to-noise-ratio in a tomographic image as $SNR = \langle I \rangle / \sigma$, where $\langle I \rangle$ denotes the image mean value in a region far from sharp interfaces, the SNR gain factor due to the phase retrieval will be:

$$\mathrm{SNR}_{\mathrm{gain}} = \frac{\mathrm{SNR}_{\mathrm{PhR}}}{\mathrm{SNR}_{\mathrm{noPhR}}} = \frac{\langle I \rangle / \sigma_{\mathrm{PhR}}}{\langle I \rangle / \sigma_{\mathrm{noPhR}}} = \left[\frac{8}{3\pi}\frac{A^2}{\ln A - 1}\right]^{1/2} \tag{5.10}$$

This equation represents a crucial result since it allows to determine the effect of all the experimental parameters, summarized by A, on the image SNR and, ultimately, on the visibility of details. Assuming that the logarithmic term varies slowly, the SNR gain increases almost linearly with the parameter A. By recalling its definition in Eq. (5.7), this means that the gain factor scales approximately linearly with the propagation distance. Considering the realistic parameters described above, the expected SNR gain is between 1 and 2 orders of magnitude, which means that phase retrieval has a dramatic impact on the image quality. A convincing experimental demonstration of this effect, based on images of rabbit kitten lungs, can be found in [5].

The effects of propagation, phase retrieval and their combination on the tomographic image signal, noise, SNR and blur are schematically summarized in Table 5.1.

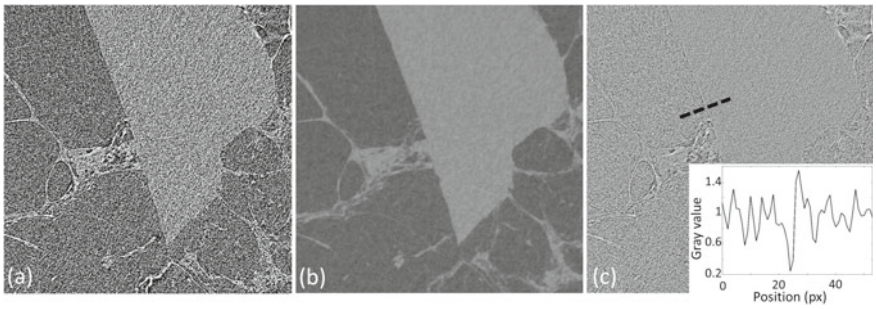

Fig. 5.1 Detail of a breast specimen PB tomographic image reconstructed without (**a**) and with (**b**) PhR. In (**c**) the ratio of (**b**) and (**a**) is reported: the application of PhR does not alter the image signal except for sharp interfaces where edge-enhancement effect is present as shown by the inset in (**c**) reporting the intensity profile along the black dashed line

Table 5.1 Schematic summary of the effects of propagation and phase retrieval on common image quality metrics. Arrows identify whether the image quality increases (green), decreases (red) or remains constant (black)

	Contrast	Noise	SNR	Blur (or resolution^{-1})
Propagation	↔	↔	↔	↓
PhR	↔	↓	↑	↑
Propagation + PhR	↔	↓	↑	↔

5.1.2 Acquisition Parameters and Image Analysis

All the acquisitions performed to test the aforementioned model have been carried out at a fixed source-to-detector distance of 31.6 m, at a beam energy of 30 keV, and by positioning the sample at 3 different object-to-detector distances, 1.6, 3 and 9 m, respectively. These sample positions correspond to geometrical magnifications $M = [1.05, 1.10, 1.40]$, and to effective propagation distances $z' = z_1/M = [1.52\,\text{m}, 2.73\,\text{m}, 6.43\,\text{m}]$. As a general remark it is worth noting that, especially at high magnifications, the actual finite dimension of the source should be taken into account since it contributes to the overall image blurring, thus reducing the spatial resolution [6], as discussed in Sect. 2.3. Anyway, considering the actual source size, which is in the order of 100 μm [7], and the small magnification factors used (1.4 or lower), the finite source size effect can be (as a first approximation) neglected since, following Eq. (2.15), its contribution is smaller than the pixel size (60 μm).

Each scan is performed in 40 s, collecting 1200 projections over 180 deg with a rotation speed of 4.5 deg s^{-1}. The fluence on the detector plane was fixed in order to deliver a total mean glandular dose of 25 mGy at the patient position, i.e. 1.6 m object-to-detector distance. It should be noted that at larger distances both the effects

of magnification and X-ray attenuation in air are not negligible and they determine a higher delivered dose. In particular, air attenuation produces a dose increase of ∼10% at 3 m and ∼45% higher at 9 m of propagation at 30 keV: considering in-vivo applications, this issue can be overcome by positioning a vacuum pipe between the object and the detector, thus avoiding air attenuation. Anyway, as it will be clear in the next section, it can be argued that both magnification and air attenuation effects are largely compensated by the SNR increase at larger distances, leaving room for the possibility of a major dose reduction.

The scanned sample is a portion of a total breast mastectomy containing an epithelial and stromal sarcomatoid carcinoma. After the formalin fixation and sealing in a vacuum bag, the sample diameter is of about 12 cm. The projection images are preprocessed as described in Chap. 4 and phase retrieved with $(\delta_1 - \delta_2)/(\beta_1 - \beta_2) = 795$ (two-materials PhR), corresponding to a glandular/adipose interface, according to the values extracted from a publicly available database [8]. CT images are reconstructed via a parallel-beam FBP with a Shepp-Logan filter, meaning that, in the model introduced in the previous section (see Eq. (5.6)), $G(U) = U\,\mathrm{sinc}(U)$ where $\mathrm{sinc}(U) = \sin(\pi x)/(\pi x)$ is the normalized sinc function. The backprojection algorithm makes use of linear interpolation, therefore $F_{\mathrm{interp}}(U) = [2 + \cos(2\pi U)]/3$. The detector MTF is modelled as a bi-dimensional sinc function, $MTF(U, V; 1) = \mathrm{sinc}(U)\,\mathrm{sinc}(V)$, which implies a bi-dimensional box-shaped point-spread-function (PSF) in real space having a width corresponding to the pixel size. The latter assumption, despite being an approximation, is rather reasonable for photon-counting detectors as Pixirad-8, where the PSF width is dominated by the physical pixel dimension, hence $d/h \simeq 1$.

As a first step of image analysis, the SNR of the images prior to the phase retrieval is measured within circular ROIs (4000 pixels each) embedded in the tumoral tissue, avoiding sharp edges. Following the model introduced in the previous section, if no phase-retrieval is applied SNR should not change significantly when the propagation distance is varied, being equal to the SNR that would be observed in the contact (i.e. object) plane, except for magnification effects.

Specifically, the SNR measured from experimental images is defined as:

$$\mathrm{SNR} = \frac{\langle I \rangle}{\sigma} \frac{M}{M_0} \sqrt{\frac{N_0}{N}} \tag{5.11}$$

where $\langle I \rangle$ is the mean pixel value, σ the standard deviation in the ROI. To compensate for geometrical magnification, SNR is normalized to the magnification M over a reference value $M_0 = 1.05$, corresponding to the patient support position (effective propagation distance of 1.52 m). A detailed justification for this normalization factor is provided in Appendix B. Moreover, to make up for small fluence variations in different acquisitions, SNR is also normalized to the square root of the average number of counts in the detector N over the reference number N_0 corresponding to the recorded counts at 1.52 m of propagation. Of note, both normalization factors are rather small numbers (their product ranges from 1 to 1.4) compared to the SNR

gain due to phase retrieval. The error associated to the SNR is given by the standard deviation of five SNR measurements performed in non-overlapping ROIs. SNR measurement is repeated on phase-retrieved images and SNR gain factor is calculated: it should be stressed that, while the introduced normalization factors play a role in calculating SNR, they are completely irrelevant for the calculation of the SNR gain factor since they cancel out as it is clear from Eq. (5.10).

Subsequently, the image contrast is measured from ROI pairs positioned both within tumor (subscript 1) and adipose (subscript 2) regions:

$$C = \frac{\langle I_1 \rangle - \langle I_2 \rangle}{\langle I_2 \rangle} \times 100 \tag{5.12}$$

Since phase retrieval affects image noise while propagation affects spatial resolution, the contrast should not change neither with the application of the phase retrieval, nor varying the propagation distance. As for the SNR, the error associated to the contrast is given by the standard deviation of five contrast values measured in non-overlapping ROI pairs.

The spatial resolution is measured for the phase-retrieved images by selecting, for each distance, three line profiles across a sharp fat/tumor interface produced by a surgical cut. The line profiles are fitted with an error function (erf) and the FWHM of its derivative is measured. The spatial resolution is evaluated as the mean value of the three FWHMs and the error is estimated to be the maximum fluctuation around the mean value. According to the theory, excluding the effect of the magnification, the spatial resolution after the PhR should not vary at different propagation distances since, for each distance, the PhR is expected to produce the same resolution that would have been measured in the contact plane image. In order to consider only the intrinsic system's spatial resolution, the FWHM is measured in number of pixels instead of an absolute length.

5.1.3 Experimental Results

Many experimental results reported in this section are reproduced from [9] by permission of IOP Publishing.

In Fig. 5.2 the reconstructed slices at all effective propagation distances (1.52 m, 2.72 m, 6.44 m) without (a)–(c) and with (d)–(f) PhR are shown. With the aim of a visualization allowing a straightforward comparison between images with and without phase retrieval, the gray levels of all the images have been scaled by a normalization factor such that the average value of fibroglandular tissue far from interfaces is 1 while air is 0. Since tissue relaxation occurred and sample repositioning was needed, some morphological changes (e.g., different position of air gaps within the tissue) are observed at different propagation distances. Care was taken to ensure the best match at all distances in the region enclosed by the dashed line of panel (a), where all the measurements are performed. From the images it can be qualitatively

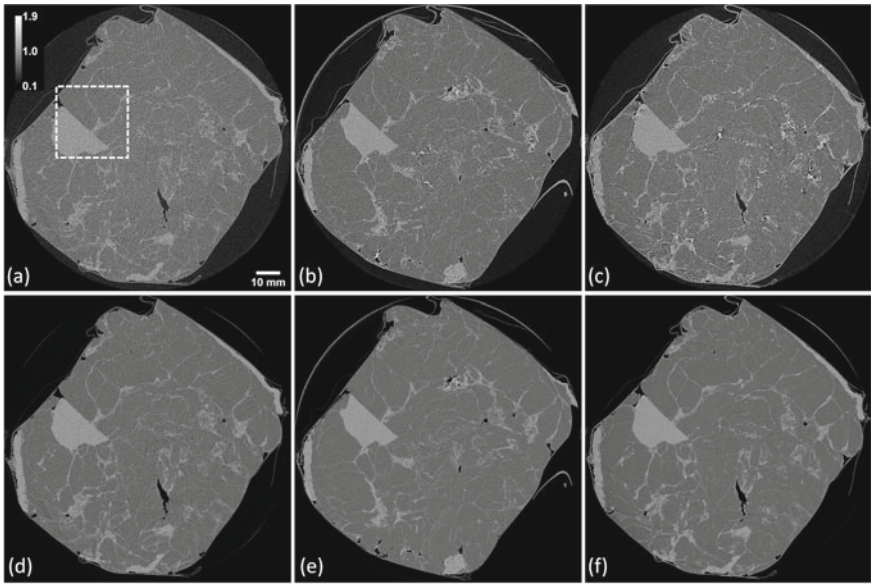

Fig. 5.2 Reconstructed slice acquired at effective propagation distances of 1.52 m (**a**), (**d**), 2.72 m (**b**), (**e**) and 6.44 m (**c**), (**f**). Images in the first row (**a**)–(**c**) are reconstructed without PhR, images in the second row (**d**)–(**f**) with PhR. The dashed square in (**a**) is the zoom region reported in Fig. 5.3. After the normalization described in text, images are displayed in a gray scale window ranging from 0 to 2, where 0 is a typical value of air and 1 a typical value of fibroglandular tissue. Morphological variations at different distances are due to sample repositioning and tissue relaxation within the sample holder

noted that, if no PhR is applied, no major variation in signal and noise is observed by varying the propagation distance, except for the sharp interfaces between adipose (dark gray) and tumor or fibroglandular (bright gray) tissue. On the contrary, when increasing propagation distances, the phase-retrieved reconstructions are smoother while no differences at tissues interfaces are observed.

The same effect is reported in a finer detail in Fig. 5.3, where a zoom on a sharp adipose/tumor interface produced by a surgical cut is displayed. Considering the non-phase-retrieved images (a)–(c) it is clear that the edge-enhancement effect at the interfaces between the two different tissues is amplified at larger propagation distances, i.e. the high-spatial frequencies are boosted. This can be better visualized in panels (g)–(i) reporting the line intensity profiles of the non-phase-retrieved images. Besides the edge-enhancement effect, clearly visible in panel (i), the profiles show a high level of noise, possibly hampering tissue differentiation. On the other hand, when the PhR is applied (d)–(f), the edge appearance does not change by varying the propagation distance and the edge-enhancement is no longer present. Considering the respective line profiles reported in panels (j)–(l), a similar edge sharpness is observed at all distances and, when compared with the non-phase-retrieved images profiles, the noise level is significantly lower.

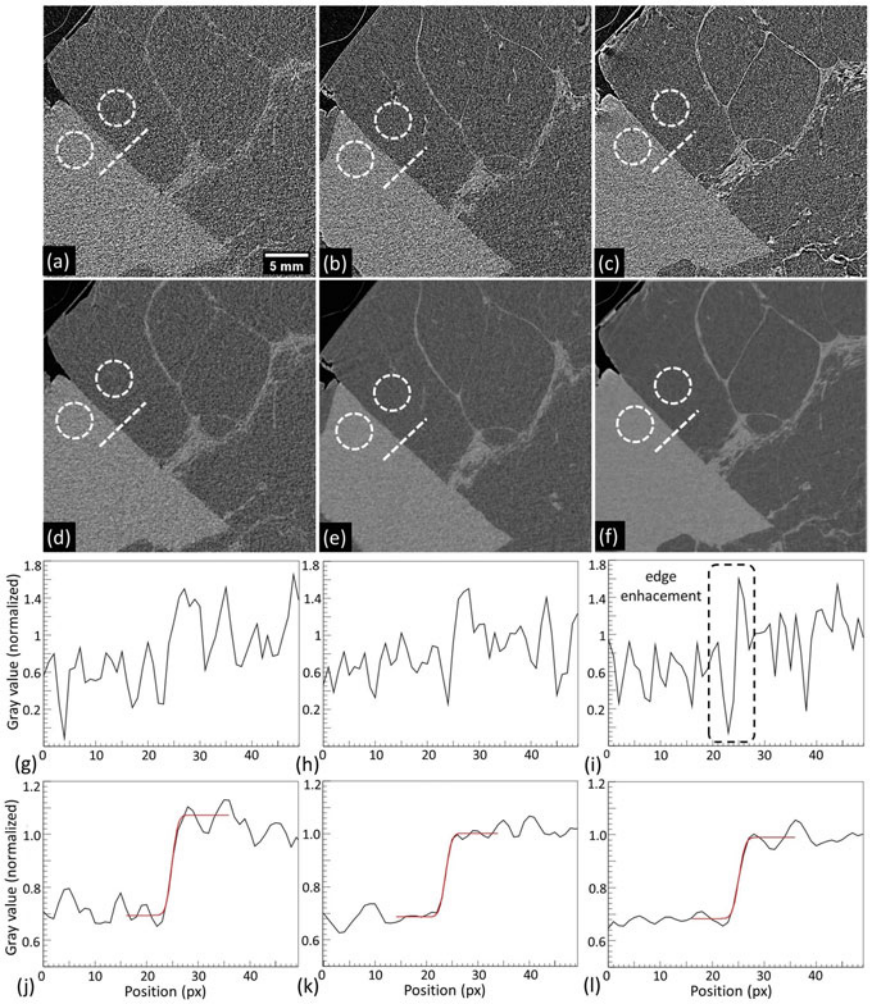

Fig. 5.3 Zoomed detail of Fig. 5.2 without (**a**)–(**c**) and with (**d**)–(**f**) phase retrieval at increasing propagation distances (from left to right). In panels (**g**)–(**i**) profiles obtained from the dashed lines in (**a**)–(**c**) are reported. In panels (**j**)–(**l**) profiles obtained from the dashed lines in (**d**)–(**f**) are reported along with the *erf* fit (red curve). In (**a**)–(**f**) one of the five pairs of circular ROIs used to determine contrast and SNR is displayed as an example

The quantitative results of the image analysis are reported in Table 5.2. As predicted by the theory (see Table 5.1) the SNR, calculated according to Eq. 5.11, does not vary significantly with the propagation distance if no PhR is applied, while its increase due to PhR is greater than a factor of 20 when considering 6.44 m of propagation distance. In addition, it must be noted that only little contrast variations (below 6%) are observed when changing the distance while, at a given position,

Table 5.2 Quantitative results. The uncertainty associated to each measure is enclosed between round brackets

	z'			
	PhR	1.52 m	2.72 m	6.44 m
SNR	No	1.63 (0.02)	1.63 (0.03)	1.62 (0.01)
	Yes	8.45 (0.13)	13.3 (0.3)	33.8 (0.7)
Contrast (%)	No	48.9 (0.5)	44.1 (0.5)	50.0 (0.4)
	Yes	48.6 (0.3)	44.2 (0.1)	49.1 (< 0.1)
FWHM (px)	Yes	2.1 (0.5)	2.3 (0.3)	2.4 (0.2)

no relevant contrast alterations are associated to the PhR algorithm whose action is limited to image noise. The latter observation is of great importance in sight of the clinical application of this technique, since the image appearance will look 'familiar' to the clinician's eye, who will not require a specific training to read the images, as it may occur for other phase-contrast techniques. Furthermore, considering phase-retrieved images, the FWHM measured in pixel units does not vary significantly with the propagation distances and, in all cases, it was found to be slightly higher than 2 pixels (120 μm on the detector plane). This implies that, taking into account the magnification, the actual spatial resolution slightly improves at longer distances (FWHM 100 μm) at the expense of a smaller field of view.

With the aim of a better data visualization, the measured SNR gain, contrast and spatial resolution concerning the phase-retrieved images (points) and the theoretical predictions (lines) are plotted as a function of the propagation distance in Fig. 5.4. From the top panel it can be seen that the measured SNR gain is in remarkable agreement with the model results obtained via numerical integration considering realistic detector and reconstruction parameters (solid line). Interestingly, if the analytical formula given in Eq. (5.10) is followed instead of numerical integration, the predicted SNR gain factor (dashed line) is about 2-fold higher than the measured one. This can be easily explained taking into account the number of simplifications made in deriving that expression, the fundamental one being the rather unrealistic assumption of a detector featuring a constant MTF up to the Nyquist frequency: for this reason the values predicted according to the analytical formula constitute, in practice, an upper limit in terms of SNR gain when compared with experimental data. At the same time, it is worth mentioning that the factor of 2 difference between the two different approaches is almost constant at all the propagation distances, hence, even if Eq. (5.10) does not provide an accurate estimate of SNR gain factors in absolute terms, it still provides the correct trend with respect to the propagation distance. In addition, when comparing phase-retrieved images, a 4-fold increase in SNR is observed at 6.44 m with respect to the shortest propagation distance (1.52 m): remarkably, at a fixed propagation distance, such SNR increase would correspond to a 16-fold higher radiation dose.

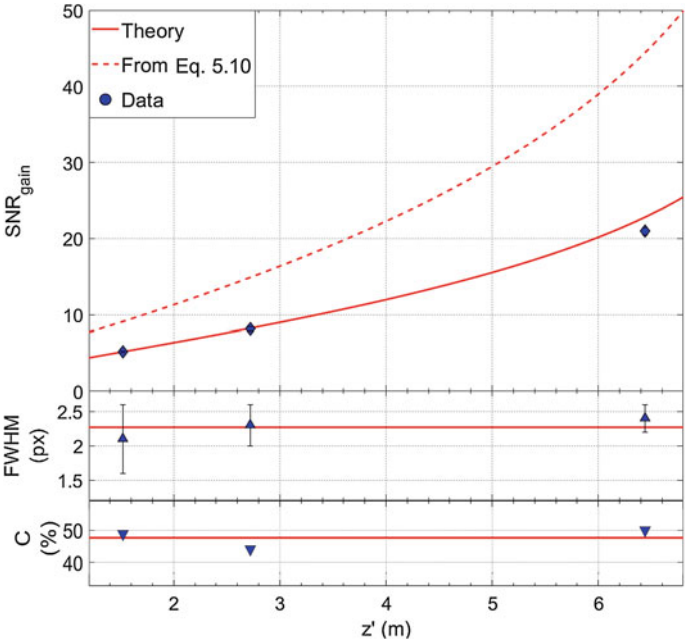

Fig. 5.4 Comparison between experimental results (points) and theoretical predictions (lines) as a function of the propagation distance. In the top panel the SNR gain factors calculated by using the analytical expression in Eq. (5.10) (dashed line) and by numerical integration from Eq. (5.8) with realistic parameters (solid line) are reported. Some error bars are smaller than points

As a final remark it is worth to mention that the model introduced and tested throughout this section is valid within the near-field propagation description or, equivalently, for large Fresnel numbers $N_F \gg 1$. Since the Fresnel number is inversely proportional to the propagation distance, this condition practically limits the maximum achievable SNR gain, which cannot arbitrarily increase. Of note, the requirement of a large Fresnel number is often relaxed in experimental practice and the near-field description is adopted even when $N_F \gtrsim 1$.

5.1.4 Consequences on the SYRMEP Upgrade

Improving any radiographic technique means either to provide a higher image quality at a constant dose or, equivalently, to provide the same image quality at a lower dose. In light of the results of the previous section, a longer propagation distance has the potential to dramatically improve PBBCT. Unfortunately, at the SYRMEP beamline, the patient support is at a fixed distance (30 m) from the source. This means that larger propagation distances can be only reached by further distancing

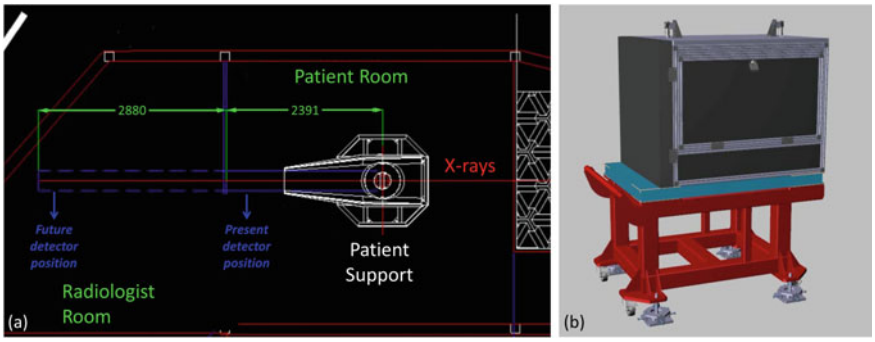

Fig. 5.5 Drawing of the patient room and the adjacent room, referred to as 'radiologist room' (**a**): dashed blue lines represent the propagation distance extension across the two rooms, allowing a gain of about 3 m in propagation distance (distances in figure are reported in mm). Drawing of the cabinet required to install the detector in the new position (**b**). The cabinet will be interlocked with the safety system constituting, in practice, an extension of the patient room

the detector from the support along the beam direction. This requires some major modifications to the present configuration of the beamline, where the maximum available sample-to-detector distance in the patient room is 1.6 m. As a consequence of the presented results, the realization of an *ad-hoc* designed extension beyond the patient room, depicted in Fig. 5.5, panel (a), has been funded. The extension will bring to a gain of about 3 m of propagation, corresponding to an object-to-detector distance of about 4.5 m. Due to radiation protection requirements, the detector will be enclosed within a dedicated cabinet, shown in panel (b), which will be interlocked with the safety system. According to the presented noise model, validated through experimental results hereby reported, this new configuration is expected to produce a SNR improvement of a factor of 2 or more with respect to the present setup at a constant fluence on the sample plane, i.e. at a constant delivered dose, thus constituting an major improvement in the SYRMA-3D project.

5.2 The Effect of Pixel Size

The other key parameter in determining the effectiveness of propagation-based imaging and phase-retrieval filtration is the detector pixel size. Intuitively this can be explained by considering that phase effects in PB imaging emphasize the sample high spatial frequencies, therefore requiring for a high spatial resolution detector. Moreover, an effective detection of edge-enhancement effects, arising upon propagation, determines the effectiveness of the subsequent phase-retrieval algorithm in producing a high SNR image without introducing an excessive smoothing. Hereinafter the notion of detector featuring a 'high spatial resolution' will be identified with 'small pixel size'. This simplification is not rigorously valid for indirect-conversion

detectors, whereas it is fairly accurate for many direct-conversion photon-counting detectors as Pixirad-8, where the PSF width is mainly determined by the pixel size. By making use of the noise model previously introduced, in this section the effect of pixel size on image noise will be studied, and theoretical results will be compared with experimental data. Some of the results hereby presented have been documented in [10].

5.2.1 *Noise Dependence on Pixel Size in Propagation-Based CT*

Regardless of the imaging modality (attenuation, propagation-based etc.) noise magnitude CT images is strongly dependent on the detector pixel size. Starting from the model described by Eq. (5.5) and isolating only the terms related to the pixel size, the variance measured in reconstructed tomographic image reads

$$\sigma^2 \propto \frac{f(A; d/h)}{h^4} \tag{5.13}$$

where the numerator is function of the pixel size only through the parameter A, as described by Eq. (5.7). When no PhR is applied (i.e. $A = 0$), as in case of conventional attenuation-based CT, the previous equation implies that image noise increases with the inverse of the square of the pixel size [4]. Given the steep dependence between image noise and pixel size, high-resolution CT images with acceptable noise levels cannot be obtained when constraints in terms of radiation dose or scan time are present, as in clinical or animal studies. Conversely, when PhR is applied (i.e. $A \neq 0$), noise dependence on the pixel size is much shallower, being mitigated by the function f, as shown in Sect. 5.1.1.2. In particular, f is monotonically decreasing for increasing values of A, hence, being $A \propto 1/h^2$, for decreasing pixel sizes.

Assuming, as done in the previous section, a bi-dimensional sinc function MTF, Shepp-Logan reconstruction filter and linear interpolation during the backprojection process, the CT image noise can be computed as a function of pixel size by making use of Eqs. (5.5) and (5.6). The numerical results, spanning a pixel size interval from 10 μm to 1000 μm and the same propagation distances reported in the previous section, are shown in Fig. 5.6: interestingly, for all propagation distances, the difference in noise between images reconstructed with or without PhR is amplified at smaller pixel sizes, meaning that the noise-reduction effect due to PhR becomes more effective as the pixel size decreases. On the other hand, at large pixel sizes, the noise level of PhR images asymptotically converge to the non-PhR case, thus the application of PhR does not entail any improvement in terms of SNR. This can be easily understood as almost no (high-frequency) phase effects arising during the propagation process can be detected if the pixel size is too large. In addition, it is worth noting that the differences in the trends of the two curves are further exacerbated by the propagation distance, coherently with the results presented in Sect. 5.1.3.

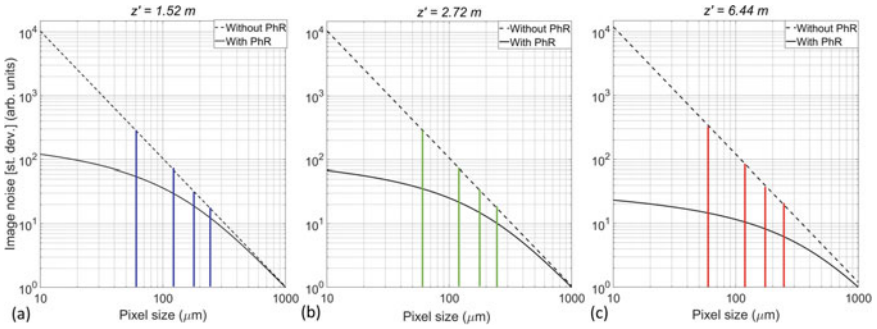

Fig. 5.6 Tomographic image noise as a function of the pixel size computed at propagation distances of 1.52 m (**a**), 2.72 m (**b**) and 6.44 m (**c**). Dashed lines refer to images without PhR, solid lines to images with PhR. For each plot the image noise has been normalized to the PhR case at pixel size of 1000 μm. Vertical lines indicate the pixel sizes of experimental data, whose results are reported in Fig. 5.8

In analogy with the limitations on the SNR increase with increasing propagation distances, the noise cannot be indefinitely decreased by having arbitrarily small pixel sizes since the presented mathematical formulation holds in the large Fresnel number approximation (N_F decreases with the square of the pixel size).

5.2.2 Noise Dependence on Pixel Size: Experimental Results

To test the effect of pixel size on experimental data, the same breast specimen presented in the previous section, scanned at three propagation distances, has been used. In order to achieve different pixel sizes projection images have been re-binned by factors of 1, 2, 3, and 4 prior to PhR, resulting in pixel pitches of 60 (native spacing), 120, 180 and 240 μm. Following the re-binning procedure, projections are processed according to the reconstruction pipeline described in Sect. 3.7, and the SNR is measured within a homogeneous glandular detail for both phase-retrieved and non-phase-retrieved datasets.

Figure 5.7 shows a detail of the reconstructed volume at different pixel pitches, both without (top row) and with (bottom row) PhR. From the images it is clear that the noise reduction due to PhR is crucial to drastically reduce image noise, thus improving detail visibility, at a pixel size of 60 μm, while its effect is less and less noticeable for larger pixel sizes. In particular, at 240 μm pixel size, phase retrieval does not produce a relevant gain in SNR and its application can be avoided without impairing the visibility of glandular structures.

From the reconstructed datasets the SNR gain factor has been computed, following the definition of Eq. (5.10), and compared with the numerical results obtained from the plots in Fig. 5.6. The comparison between the model predictions and the experimental data is reported in Fig. 5.8. From the plot an excellent agreement between

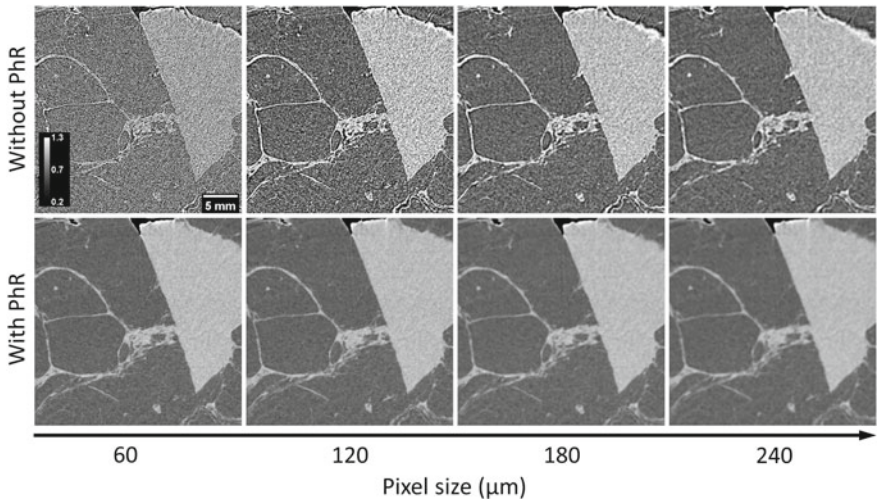

Fig. 5.7 Crop of a reconstructed tomographic slice showing a fibroglandular detail embedded in adipose background acquired at 6.44 m of propagation distance. Each column refers to a given pixel size while each row specifies whether the PhR is applied or not. All the images are windowed on the same gray level scale (inset of the top-left image) to facilitate the comparison. Reproduced from [10] by permission of IOP Publishing

model and data is observed for all propagation distances. Of note, the experimental points obtained with the 60 μm pixel pitch correspond to the ones in Fig. 5.4, where the dependence on propagation distance was studied. It is interesting to observe that the increase in the pixel size is associated to a major decrease of the SNR gain due to PhR. This trend is more pronounced for larger propagation distances: specifically, at 6.44 m the gain increases by a factor of 7 going from the largest to the smallest pixel pitch, while at 1.52 m its increment is in the order of a factor 3.5.

In light of the results presented in this section, which are supported by a rigorous mathematical model, it is clear that going towards small pixel sizes is crucial to fully exploit the noise reduction capabilities of phase retrieval. Going back to the problem of achieving low-dose tomographic images with a high spatial resolution, the use of propagation-based imaging coupled with a small pixel size detector can be an invaluable tool to overcome, or at least mitigate, visibility issues related to excessive image noise. In this context, the development of high-efficiency photon counting detector with smaller pixels, coupled with suitable on-chip processing strategies to compensate for charge sharing effects [11, 12], will be of great importance for a wider and more efficient use of PB imaging in biomedical applications.

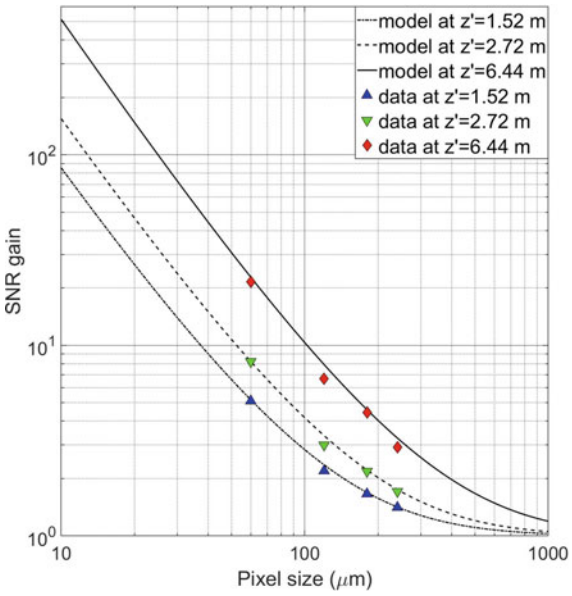

Fig. 5.8 SNR gain as function of pixel size derived from experimental data (points) and from the theoretical model (lines) at three propagation distances

5.3 Beam Profile Optimization: Flattening Filter

In addition to the high coherence, X-rays produced by synchrotrons are generally several orders of magnitude more intense with respect to conventional sources. For this reason, many bio-medical imaging applications, as BCT, require beam filtration to deliver acceptable dose levels [13, 14]. As described in Sect. 3.6, this is typically performed by inserting aluminum sheets or slabs that reduce the overall beam intensity without affecting its spatial distribution (or 'shape'). Specifically, the vertical (i.e. orthogonal to the electrons' orbit plane) intensity profile of a synchrotron beam produced by bending magnets can be described by a Gaussian distribution [15]. This leads to an undesired non-uniform dose distribution on the sample in the vertical direction. In terms of image quality, this translates into a non constant SNR, which decreases moving from the central maximum of the beam towards the tails. To limit such non-uniformity, in many experiments only the central part of the beam is used for imaging purposes, while the tails are filtered out by absorbing (e.g., made of tungsten) slits. Despite being easy to implement, this approach is not optimal in sight of any application, especially in-vivo, requiring the scan of large samples as the reduction of the vertical beam dimension entails an increase in the number of vertical scans required to image a large volume and, as a consequence, an increase in the overall scan duration.

To overcome the non-uniformity, while using the full beam vertical dimension, an *ad-hoc* parabolic shaped flattening filter has been designed and implemented. Up to now, a slit system made of Densimet® (tungsten alloy), coupled with planar aluminum filters, has been routinely used. This system defines a vertical beam

dimension of 3.5 mm at sample position encompassing intensity variations of about 30% at energies around 30 keV. Conversely, the new filtration system produces a nearly constant vertical intensity distribution, allowing uniform radiation dose delivery, hence yielding tomographic images with uniform SNR, as well as to use of a wider vertical portion of the beam (5 mm or more), allowing for scan time reduction for large samples. It should be noted that, as the filter development is one of the latest improvements of the BCT experimental setup, most of the images presented in this thesis were acquired using the conventional slits/planar filtration system. Many results presented in this section are also documented in [16].

5.3.1 Filter Design

A flat transmitted intensity distribution is obtained for a filter, described by the function $F(y; E)$, satisfying the following equation:

$$I_f(y) = I(y; E)e^{-\mu_f(E)F(y;E)} = k \tag{5.14}$$

where $I(y, E)$ is the incoming beam intensity distribution along the vertical direction y, $\mu_f(E)$ is the energy (E) dependent attenuation coefficient of the filter and $I_f(y)$ is the flattened transmitted beam, whose intensity is equal to a transmitted fraction k of the maximum of the input beam. By assuming that the unfiltered beam has a Gaussian vertical spatial distribution, $I(y; E) \propto \exp\left(-\frac{y^2}{2\sigma_y^2(E)}\right)$, with an energy dependent standard deviation $\sigma_y(E)$, the filter shape can be computed by solving Eq. (5.14), and it reads

$$F(y; E) = -\frac{y^2}{2\sigma_y^2(E)\mu_f(E)} - \frac{\ln k}{\mu_f(E)} \tag{5.15}$$

Therefore, the desired filter has a parabolic shape whose depth (d_f, i.e. size along the beam propagation direction) and height (h_f, i.e. size along the vertical dimension of the beam) are, respectively

$$d_f = \frac{|\ln k|}{\mu_f(E)}, \quad h_f = 2\sigma_y(E)\sqrt{2\,|\ln k|} \tag{5.16}$$

At this point it can be noted that the filter depth depends both on the filter material, through its attenuation coefficient, and on the desired intensity fraction of the impinging beam. Conversely, the filter height is dependent on the beam's vertical dimension and its intensity fraction while it is independent of the filter material.

The implemented filter is made of aluminum and it has been designed for an energy of 30 keV. The beam standard deviation at sample position, i.e. 30 m from the X-ray source, corresponding to 30 keV is $\sigma_y(30\text{ keV}) = 1.8$ mm. Since the filter is

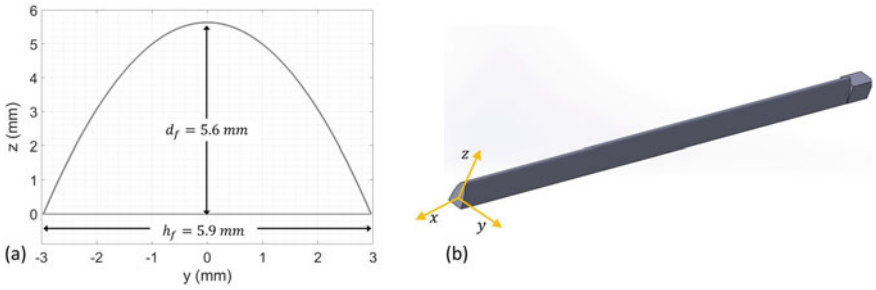

Fig. 5.9 Filter parabolic profile optimized for 30 keV beam and 26 m from the source at SYRMEP beamline (**a**) and its CAD design (**b**)

positioned 4 m upstream with respect to the sample, a standard deviation of 1.6 mm has been considered to compensate for the beam magnification. The transmission factor is chosen to be $k = 18$ %, providing sufficient flux for delivering (mean glandular) dose rates up to 0.5 mGy/s to large (∼10 cm) breast samples. Considering the standard scan time (40 s) for acquiring BCT images, this results in doses up to 20 mGy, which corresponds to the 'high-image quality' (dedicated to surgical specimens) modality of the SYRMA-3D protocol [17]. For this reason, extra filtration composed of aluminum sheets is needed to match the clinical target dose level of 5 mGy for in-vivo applications. Given k and σ parameters, the filter has been modelled via a computer-aided design (CAD) software and manufactured with a computer numerical control machine (see Fig. 5.9).

As a general remark, the energy dependence of the filter shape can be viewed as a practical drawback since, in principle, each energy would require a dedicated design. As it will be clarified in the next section, the proposed filter is proven to be sufficiently flexible for energies around 30 keV. In fact, the filter yields a beam which is more homogeneous with respect to the standard planar filtration system in a range of energies between 28 and 32 keV, which is of interest for the breast CT application. If a similar degree of flexibility is desired at lower energies, the same filtration approach could be adapted by using lighter filtering materials, whose attenuation coefficient is Compton dominated. As an example, plastic filters (i.e. $6 < Z_{eff} < 7$) would offer some energy flexibility down to about 20 keV.

5.3.2 Filter Tests in Planar and Tomographic Configurations

The flattening filter has been tested at 3 different energies of 28, 30, and 32 keV. As shown in Fig. 5.10, when used at the design energy of 30 keV (panels (b) and (e)), the filter ensures a beam profile with intensity fluctuations up to 5% and a height of 5.5 mm, whereas the unfiltered beam (a) has, in the same spatial range, a maximum intensity variation of more than 60% around the mean value. Moreover, even

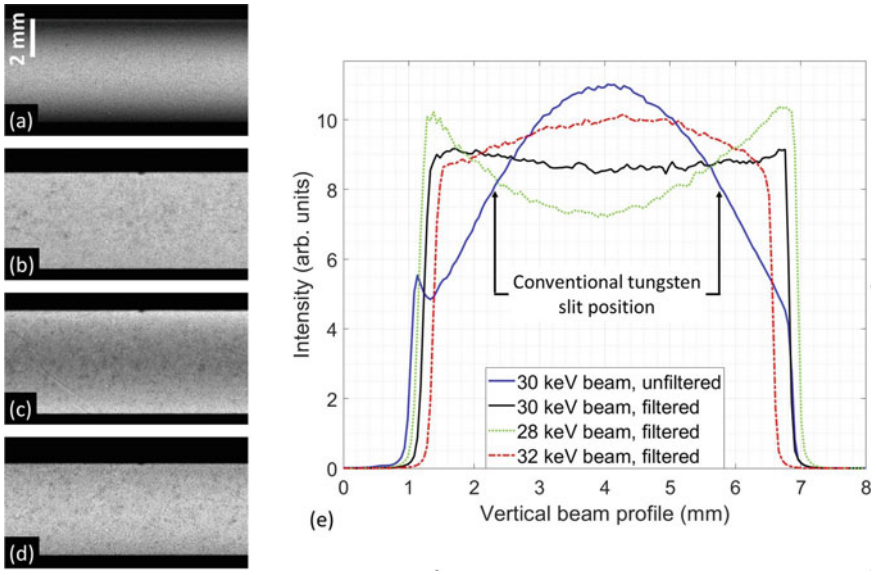

Fig. 5.10 Images of the beam with no filtration (**a**) and flattening filter at 30 keV (**b**), 28 keV (**c**) and 32 keV (**d**). Vertical profiles (**e**) of the beams reported in panels (**a**)–(**d**). Black arrows the position corresponding to the tungsten slits system used for the clinically-oriented imaging acquisitions so far. Profiles in (**e**) are normalized to their area

considering only the portion of the beam (3.5 mm) that would have been transmitted by the slit system, the intensity variation in the unfiltered beam is still around 30%. When employed at a beam energy of 28 keV (c), the filter introduce an excessive attenuation in the central part, yielding a cup-shaped profile. Anyway, the observed intensity variation over the entire beam height (5.7 mm) is of the order of 30%, that is half of the variation of the unfiltered beam in the same spatial range. The opposite behaviour is found for the 32 keV irradiation (d): in this case the maximum intensity fluctuation across the whole beam height (5 mm) is of the order of 15%, about 4 times smaller if compared to the unfiltered beam.

To demonstrate the effectiveness of the filter in a realistic scenario, the tomographic reconstructions of two mastectomy samples with similar sizes, imaged with and without using the flattening filter, have been compared. Coherently with all the scans presented in the next chapter, 5 mGy of mean glandular dose were delivered to both samples while the selected scan energy was 32 keV (which is not the optimal energy for the described filter). The results are summarized in Fig. 5.11 showing, in panels (a), (b), the reconstructed details of the sample acquired with no flattening filter, considering slices corresponding to the central and the tail regions of the beam, respectively. In the same way, panels (c), (d) show slices of the sample acquired with the flattening filter at the center and at the edge positions of the beam. For both samples, the SNR, defined as the ratio between the mean and the standard deviation of gray values within a selected region of interest, is measured within a glandular

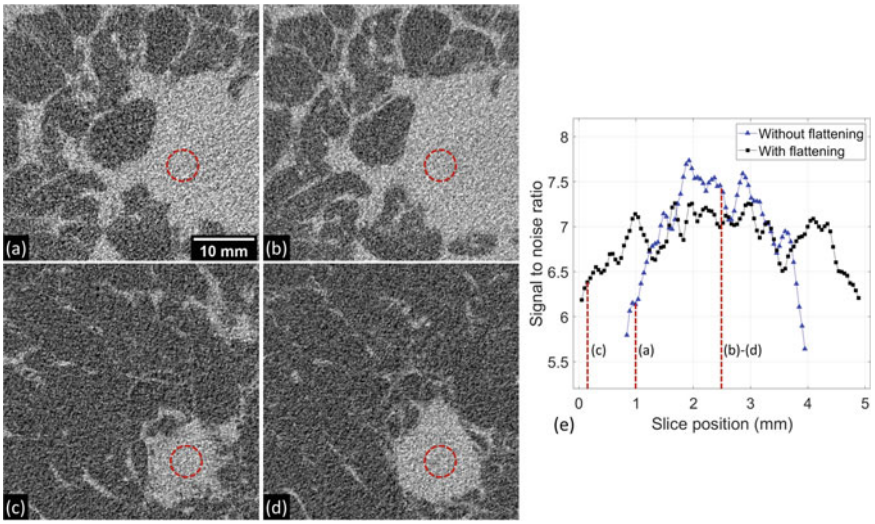

Fig. 5.11 Details of reconstructed slices corresponding to the central portion and to the edge of the vertical field-of-view obtained with conventional planar filtration system ((**a**) edge, (**b**) center) and with the flattening filter ((**c**) edge, (**d**) center), respectively. Plot of SNR as a function of slice position measured within the dashed circles in (**a**)–(**d**) for both filtering configurations. Light-blue dashed lines represent slice positions of panels (**a**)–(**d**)

detail as a function of the slice position, as reported in panel (e). As the plot shows, the use of the flatting filter brings to a smoother dependence of the SNR on the slice position compared to the conventional planar filtration. Because the flattening filter allows for a more even distribution of the radiation dose, the measured SNR is lower in the center and higher at the edges of the beam with respect to the conventional filtration case. Moreover, the wider portion of the beam useful for imaging (from slightly more than 3 mm to 5 mm for the case reported in Fig. 5.11e) translates into a reduction of the scan time for imaging the whole volume of approximately 40%. This is of great importance in view of the clinical implementation, as it will limit patient discomfort, thus motion-related artifacts, and it will improve the examination throughput.

5.4 Post-reconstruction Phase Retrieval in Multi-stage Scans

As described in the previous section, the limited vertical dimension of synchrotron X-ray beams usually requires multiple vertical steps (or stages) to image large samples, as in the BCT case. Moreover, photon-counting detectors are usually composed by mono-dimensional arrays of individual sensors few centimeters in height, thus

requiring vertical stepping even in case of an arbitrarily wide X-ray beam. In this context, the conventional reconstruction pipeline can introduce artifacts at the margins of each vertical step mainly due to boundary effects arising in the application of the phase-retrieval algorithm. In this section a post reconstruction three-dimensional PhR approach is introduced, and its ability to cope with these artifacts is demonstrated. After the demonstration of its theoretical equivalence with the conventional PhR pipeline, its effectiveness on experimental images is demonstrated. Some of the reported experimental results have been published in [18].

5.4.1 *Equivalence of Pre- and Post-reconstruction Phase Retrieval*

As mentioned in Sect. 2.6, it is common practice to apply a bi-dimensional phase-retrieval filter to each flat-corrected projection prior to the actual reconstruction. However, it can be shown that applying a three-dimensional version of the phase-retrieval filter after tomographic reconstruction leads to theoretically equivalent results. Intuitively, this can be understood as both PhR and tomographic reconstruction are linear (and commutative) filters in the Fourier space. A rigorous formal demonstration of this has been given by Ruhlandt and Salditt [19] under the 'weak object' approximation, which assumes both attenuation and phase-shift terms in the complex transmission function to be small (see Eq. (2.4)).

Actually, when dealing with near-field PB imaging and Paganin's PhR algorithm, the weak attenuation assumption can be dropped and the mathematical formulation of the three-dimensional PhR filter can be derived *mutatis mutandis* from the bi-dimensional case. In fact, in Sect. 2.6 it was shown that, under the weak phase contrast hypothesis, the tomographic map obtained from PB (i.e. with no PhR) projections can be written as

$$o^{\mathrm{PB}}(x, y, z) = \mu(x, y, z) - z_1 \nabla^2_{xyz} \delta(x, y, z) \tag{5.17}$$

At this point the homogeneous object condition (i.e. δ/β is a known constant parameter) can be inserted and, by conveniently re-writing $\delta = \delta\mu/(2k\beta)$, the previous equation becomes

$$o^{\mathrm{PB}}(x, y, z) = \left[1 - \frac{z_1 \delta}{2k\beta} \nabla^2_{xyz}\right] \mu(x, y, z) \tag{5.18}$$

where the term enclosed in square brackets is immediately identified with the three dimensional version of the froward propagation operator (H) defined in Eq. (2.23). In other words, Eq. (5.18) mathematically describes the propagation of the entire three-dimensional object in the near field which is equivalent to the propagation of each individual bi-dimensional projection. Following this analogy, the inverse operator, that is the phase retrieval, will simply be the three-dimensional extension of the expression reported in Eq. (2.24):

Fig. 5.12 Collage of a sample projection for each of the ten considered vertical stages. Due to the limited vertical size of the beam, the height of each projection consists in 51 pixels. The projections cannot be easily stitched together to compose a single projection of 510 pixels height because of the unknown angular shift and actual angular range covered induced by the continuous mode acquisition: the registration is performed within the reconstruction step

$$\tilde{H}_{3\mathrm{D}} = \left[1 + \frac{z_1 \delta}{2k\beta}(v_1^2 + v_2^2 + v_3^2)\right]^{-1} \tag{5.19}$$

where (v_1, v_2, v_3) are the Cartesian coordinates in the three-dimensional Fourier space.

5.4.2 *Bi- Versus Three-Dimensional Phase Retrieval Pipelines*

When a large volume is scanned with multiple vertical stages, suitable strategies are required for the inherent issue of image stitching [20, 21] in order to correctly create the reconstructed volume of the whole object. Projection stitching typically requires the determination of the center of rotation and in practical multi-stage tomography it might slightly vary from one vertical stage to another. Moreover, when considering continuous acquisition mode as in the case of BCT, the determination of the exact angular range covered by the scan is needed for the stitching procedure and, in general, it is different for each stage, as reported, for instance, in Fig. 5.12. Both these issues are usually tackled by registering and stitching the reconstructed slices rather than operating on the projections. As aforementioned, such a procedure implies that the PhR is applied independently to each projection of each vertical stage, generally introducing periodic artifacts in the lateral views of the tomographic volume, in correspondence with the junction slices between two adjacent stages. The reason for those artifacts lies in the absence of knowledge about the neighboring pixels of the upper and lower part of each projection image when applying the bi-dimensional (2D) independent stage-by-stage processing. In facts, the 2D PhR approach cannot consider the real information coming from the adjacent vertical stages. In most cases this shortcoming is partly overcome by replicate padding of each projection

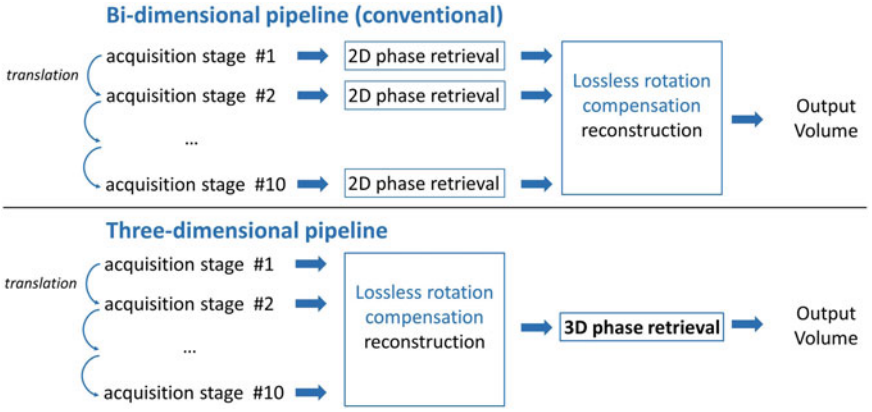

Fig. 5.13 Sketch of the two computational pipelines compared in this section. The term 'lossless rotation compensation' refers to the angular offset to be specified as additional input to the reconstruction algorithm. In this way image registration is performed by 'rolling' the sinogram to match a desired rotation angle without requiring any image interpolation

which mitigates for the absence of this information. On the other hand, the post-reconstruction three-dimensional (3D) PhR pipeline allows to perform the phase retrieval on the whole volume after the registration of each reconstructed vertical stage, thus inherently solving the missing information issue. A sketch of both 2D and 3D PhR pipelines is shown in Fig. 5.13.

5.4.3 Quantitative Comparison on a Large Breast Specimen

To demonstrate the effectiveness of the post-reconstruction 3D PhR, the two processing pipelines have been compared, based on images of a large mastectomy specimen. The sample, featuring a diameter of 9 cm and a height of 3 cm, contained an infiltrating ductal carcinoma with a diameter of about 1.2 cm. After positioning the sample in the patient support (1.6 m of propagation distance), it was scanned at 38 keV with 10 vertical steps. Each of the 1200 angular projections acquired for every vertical position was cropped to a dimension 2150×51 pixels, resulting, after the stitching procedure, in a final volume of $2150 \times 2150 \times 510$ voxels.

The set of projections was processed following either the 2D PhR or the 3D PhR pipelines (two-materials PhR, $(\delta_1 - \delta_2)/(\beta_1 - \beta_2) = 1083$). The two reconstructed volumes have been quantitatively compared in terms of spatial resolution, contrast (C) and contrast-to-noise ratio (CNR) by considering the central slice of a given 51 slices stack. Spatial resolution was measured, as described in Sect. 5.1.2, starting from the three intensity profiles reported in blue in Figs. 5.14 and 5.15. The two circular regions (one within glandular tissue referred to as A and the other one within adipose tissue referred to as B) reported in the same figures were used to compute the mean

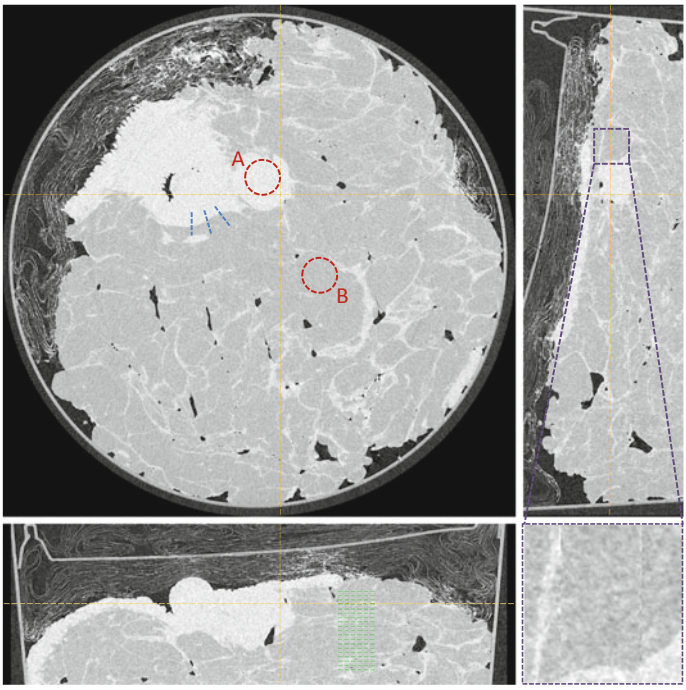

Fig. 5.14 Orthogonal views of the output volume when the pipeline with 2D phase retrieval is applied. A close-up (bottom-right) is reported to highlight the observed artifact at the interfaces between adjacent vertical stages. Colored segments or ROIs were used for quantitative analysis as described in text

$\langle I \rangle$ and the standard deviation σ of the gray levels. From these quantities the contrast was determined as reported in Eq. (5.12), while the CNR was computed as

$$\text{CNR} = \frac{\langle I_A \rangle - \langle I_B \rangle}{\sigma_b} \tag{5.20}$$

In addition to these metrics, with the aim of highlighting the artifact at the interface of adjacent reconstructed stages, the standard deviation measured from a line ROI covering 121 voxels (green lines in Figs. 5.14 and 5.15) was evaluated for each reconstructed slice and plotted against the corresponding vertical position.

Figures 5.14 and 5.15 show the transverse, i.e. orthogonal to the rotation axis, and lateral views of the entire reconstructed volume for the 2D and 3D PhR cases, respectively. When comparing the transverse slices, which correspond to the center of a vertical stage, almost no differences between the two pipelines are observed. This qualitative evaluation is confirmed by the numerical results of the quantitative analysis, summarized in Table 5.3. The analysis revealed almost identical spatial resolution, contrast and CNR for both the considered cases. For the sake of com-

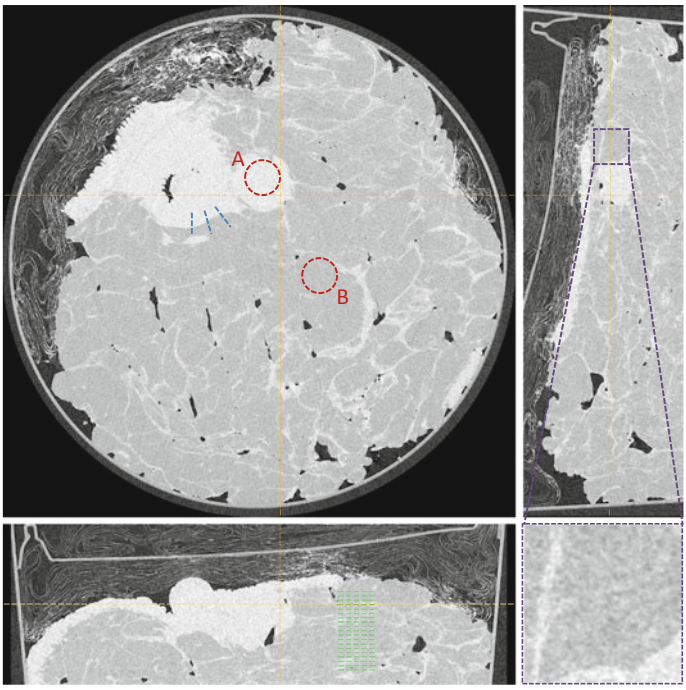

Fig. 5.15 Same as Fig. 5.14 but reconstructed through the 3D phase retrieval. The close-up shows the lack of artifacts between adjacent vertical stages

Table 5.3 Quantitative comparison between 2D and 3D phase-retrieval pipelines

	Spatial resolution FWHM (mm)	Contrast C (%)	Contrast-to-noise ratio CNR
2D pipeline	0.117 ± 0.025	34.4	3.46
3D pipeline	0.118 ± 0.025	34.3	3.46

pleteness the line profiles along with the fit functions used to estimate the spatial resolution are reported in Fig. 5.16: of note is that, considering an effective pixel size of 57 μm, the values of FWHM found in this analysis well compares with the ones reported in Sect. 5.1.3.

While the two approaches yield substantially identical results when considering transverse slices far from the margins of a vertical stage, as anticipated from the formal equivalence between 2D and 3D PhRs, major differences are found in the junction slices across two stitched vertical stages. This can be observed in the close-up images of Figs. 5.14 and 5.15 (bottom-right panels) and, quantitatively, from the plot reported in Fig. 5.17, where a periodic spike in the measured standard deviation can be clearly noticed every 51 slices in the case of the pre-reconstruction 2D PhR approach, while no artifacts are visible in the post-reconstruction 3D PhR case. Of note, for all the transitions across different stages, the artifact involves 3 or 4 slices,

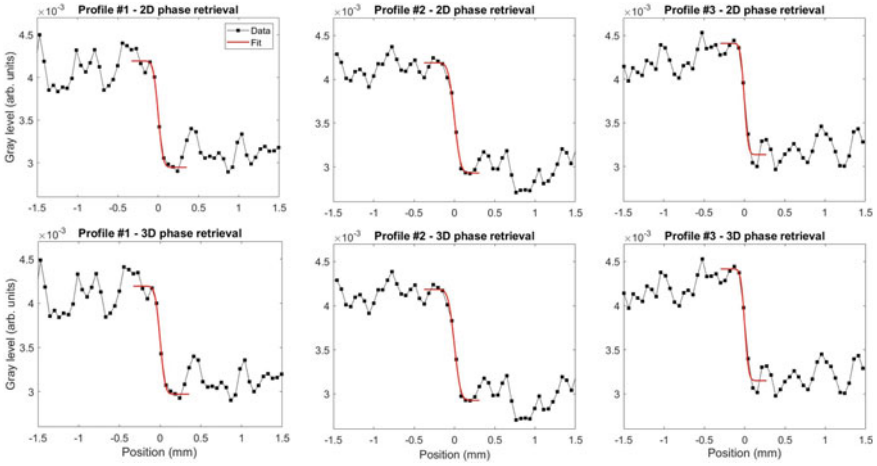

Fig. 5.16 Plots of the fit used for the assessment of the spatial resolution on a reconstructed slice for the 2D case (top row) and 3D case (bottom row). The three considered profiles are highlighted in blue in Figs. 5.14 and 5.15

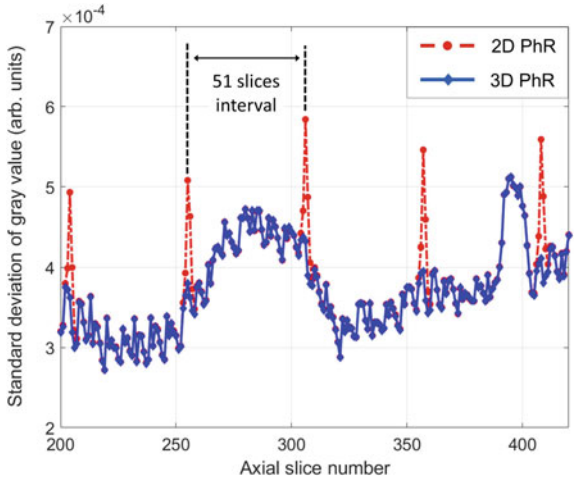

Fig. 5.17 Plot of the standard deviation of the gray levels with reference to the green lines in Figs. 5.14 and 5.15. A spike every 51 slices is noticeable for the 2D phase retrieval

meaning that, given the displacement dimension of the considered vertical stages, about 6 to 8% of the volume presents an undesired increase of noise due to the bi-dimensional pipeline. As previously mentioned, the advantage of 3D PhR over the 2D approach is the possibility of using the whole object information by filtering the reconstructed volume rather then relying on a single, vertically limited projection.

It should be stressed that, if a full-height (510 pixels) projection could be composed by tiling each vertical stage, this artifact would result similarly compensated through the conventional 2D PhR approach. However, several factors hamper this stitching process. Firstly, alignment issues due to imperfect relative positioning of

detector and rotating stage are usually better compensated during the reconstruction step with inspection of the computed images. As a matter of fact, recognizing geometrical misalignment from the input projections only is a difficult task. Moreover, the combination of continuous rotation acquisition mode with the limited precision of rotating stage motors (e.g., backlash effect) often determines an unknown relative angular shift at each vertical position. In this context, the identification of the exact projection from a given vertical position acquisition to be combined with the other vertical stages requires horizontal flipping. Depending on whether the angular shift is positive or negative, this procedure is needed at least for some of the projections either at the beginning or at the end of each scan. The flipping, in turn, requires knowledge of the center of rotation: automatic methods for its the determination exist [22], but it is common practice to assess its correctness visually, by performing a few test reconstructions of just one slice. Moreover, given that automatic methods require projections at 0 and 180 degrees as input, they may fail if the complete/exact coverage of 180 degrees is not granted, which might happen in continuous acquisitions (e.g., in BCT case). Alternatively, image correlation techniques can be used for automatic angular shift assessment, but the correctness of their output is usually better supervised by an expert user checking a reconstructed slice rather than projections. For these reasons, the application of the conventional 2D phase-retrieval to a set of stitched projections requires in any case some preliminary reconstruction. The 3D phase-retrieval approach allows to skip the stitching phase and the related challenges.

Although an accurate comparison of the two approaches in terms of computational efficiency is beyond the scope of this section, some qualitative evaluations can still be made. As the 2D PhR is, in principle, an on-line process, it can be applied as soon as each projection is collected without waiting for the acquisition of the whole tomographic dataset, resulting in a faster experimental pipeline. However, this procedure is seldom used in experimental practice. On the other hand, the 3D approach requires the whole reconstructed volume as input, which means waiting for the collection of all the projections (off-line procedure). Additionally, since the whole volume has to be loaded for processing, 3D phase retrieval requires a large amount of memory. For instance, the stacked volume considered in this section is composed of $2150 \times 2150 \times 510$ voxels, which means a 32-bit floating point matrix of about 8.8 GB. Furthermore, given that 3D phase retrieval relies on three-dimensional Fourier filtering, 3D signal padding is fundamental to avoid cross-talk between opposite sides of the volume. Compared with the 2D case, where for each projection only horizontal and vertical padding is performed, the 3D padding accounts also for an additional dimension, leading to a larger number of matrix elements to be processed. For this reason, post-reconstruction PhR can be generally considered more computationally demanding if compared to the conventional approach, therefore its use must be evaluated depending on available computational power and dataset dimension.

References

1. Nesterets YI, Gureyev TE (2014) Noise propagation in X-ray phase-contrast imaging and computed tomography. J Phys D: Appl Phys 47(10):105402. https://doi.org/10.1088/0022-3727/47/10/105402
2. Gureyev TE, Nesterets YI, Kozlov A, Paganin DM, Quiney HM (2017) On the "unreasonable" effectiveness of transport of intensity imaging and optical deconvolution. JOSA A 34(12):2251–2260. https://doi.org/10.1364/JOSAA.34.002251
3. Nesterets YI, Gureyev TE, Dimmock MR (2018) Optimisation of a propagation-based X-ray phase-contrast micro-CT system. J Phys D: Appl Phys 51(11):115402. https://doi.org/10.1088/1361-6560/aa5d3d
4. Davis GR (1994) The effeCT of linear interpolation of the filtered projections on image noise in X-ray computed tomography. J X-ray Sci Technol 4(3):191–199. https://doi.org/10.3233/XST-1993-4303
5. Kitchen MJ, Buckley GA, Gureyev TE, Wallace MJ, Andres-Thio N, Uesugi K, Yagi N, Hooper SB (2017) CT dose reduction factors in the thousands using X-ray phase contrast. Scient Reports 7(1):15953. https://doi.org/10.1038/s41598-017-16264-x
6. Gureyev TE, Nesterets YI, Stevenson AW, Miller PR, Pogany A, Wilkins SW (2008) Some simple rules for contrast, signal-to-noise and resolution in in-line X-ray phase-contrast imaging. Opt Exp 16(5):3223–3241. https://doi.org/10.1364/OE.16.003223
7. SYRMEP. SYRMEP specifications (2016). www.elettra.trieste.it/lightsources/elettra/elettra-beamlines/syrmep/specification.html
8. Taylor JA (2018) TS imaging. http://ts-imaging.science.unimelb.edu.au/Services/Simple/
9. Brombal L, Donato S, Dreossi D, Arfelli F, Bonazza D, Contillo A, Delogu P, Di Trapani V, Golosio B, Mettivier G et al (2018) Phase-contrast breast CT: the effect of propagation distance. Phys Medi Biol 63(24): 24NT03. https://doi.org/10.1088/1361-6560/aaf2e1
10. Brombal L (2020) Effectiveness of x-ray phase-contrast tomography: effects of pixel size and magnification on image noise. J Instrum 15(01):C01005. https://doi.org/10.1088/1748-0221/15/01/C01005
11. Di Trapani V, Bravin A, Brun F, Dreossi D, Longo R, Mittone A, Rigon L, Delogu P (2018) Characterization of noise and efficiency of the pixirad-1/pixie-iii cdte x-ray imaging detector. J Instrum 13(12):C12008. https://doi.org/10.1088/1748-0221/13/12/C12008
12. Gimenez E, Ballabriga R, Campbell M, Horswell I, Llopart X, Marchal J, Sawhney K, Tartoni N, Turecek D (2011) Study of charge-sharing in medipix3 using a micro-focused synchrotron beam. J Instrum 6(01):C01031. https://doi.org/10.1088/1748-0221/6/01/C01031
13. Bravin A, Coan P, Suortti P (2012) X-ray phase-contrast imaging: from pre-clinical applications towards clinics. Phys Med Biol 58(1):R1. https://doi.org/10.1088/0031-9155/58/1/R1
14. Rigon L (2014) X-ray imaging with coherent sources. In: Brahme A (ed) Comprehens Biomed Phys 2:193–216. Elsevier. https://doi.org/10.1016/B978-0-444-53632-7.00209-4
15. Viccaro PJ (1991) Power distribution from insertion device X-ray sources. In: Advanced X-Ray/EUV radiation sources and applications, vol 1345, pp 28–38. International Society for Optics and Photonics. https://doi.org/10.1117/12.23298
16. Donato S, Arfelli F, Brombal L, Longo R, Pinto A, Rigon L, Dreossi D (2020) Flattening filter for gaussian-shaped monochromatic x-ray beams: an application to breast computed tomography. J Synchrotron Radiat in press. https://doi.org/10.1107/S1600577519005502
17. Piai A, Contillo A, Arfelli F, Bonazza D, Brombal L, Cova MA, Delogu P, Trapani VD, Donato S, Golosio B, Mettivier G, Oliva P, Rigon L, Taibi A, Tonutti M, Tromba G, Zanconati F, Longo R (2019) Quantitative characterization of breast tissues with dedicated CT imaging. Phys Med Biol 64(15):155011. https://doi.org/10.1088/1361-6560/ab2c29 Aug
18. Brun F, Brombal L, Di Trapani V, Delogu P, Donato S, Dreossi D, Rigon L, Longo R (2019) Post-reconstruction 3D single-distance phase retrieval for multi-stage phase-contrast tomography with photon-counting detectors. J Synchrotron Radiat 26(2). https://doi.org/10.1107/S1600577519000237

19. Ruhlandt A, Salditt T (2016) Three-dimensional propagation in near-field tomographic X-ray phase retrieval. Acta Crystallographica Sect A: Foundat Adv 72(2):215–221. https://doi.org/10.1107/S2053273315022469
20. Kyrieleis A, Ibison M, Titarenko V, Withers P (2009) Image stitching strategies for tomographic imaging of large objects at high resolution at synchrotron sources. Nucl Instrum Methods Phys Res Sect A: Acceler Spectromet Detectand Assoc Equip 607(3):677–684. https://doi.org/10.1016/j.nima.2009.06.030
21. Vescovi R, Du M, Andrade VD, Scullin W, Gürsoy D, Jacobsen C (2018) Tomosaic: efficient acquisition and reconstruction of teravoxel tomography data using limited-size synchrotron X-ray beams. J Synchrotron Radiat 25(5). https://doi.org/10.1107/S1600577518010093
22. Vo NT, Drakopoulos M, Atwood RC, Reinhard C (2014) Reliable method for calculating the center of rotation in parallel-beam tomography. Opt Express 22(16):19078–19086. https://doi.org/10.1364/OE.22.019078